

Spectroscopy of the Young Stellar Association *Price-Whelan 1*:  
Origin in the Magellanic Leading Arm and Constraints on the Milky Way Hot Halo

DAVID NIDEVER,<sup>1,2</sup> ADRIAN M. PRICE-WHELAN,<sup>3,4</sup> YUMI CHOI,<sup>1,5</sup> RACHAEL L. BEATON,<sup>4,6,\*</sup> TERESE T. HANSEN,<sup>7</sup>  
DOUGLAS BOUBERT,<sup>8</sup> DAVID AGUADO,<sup>8</sup> RANA EZZEDDINE,<sup>9</sup> SEMYEONG OH,<sup>8</sup> AND N. WYN EVANS<sup>8</sup>

<sup>1</sup>*Department of Physics, Montana State University, P.O. Box 173840, Bozeman, MT 59717-3840*

<sup>2</sup>*National Optical Astronomy Observatory, 950 North Cherry Ave, Tucson, AZ 85719*

<sup>3</sup>*Center for Computational Astrophysics, Flatiron Institute, 162 Fifth Avenue, New York, NY 10010, USA*

<sup>4</sup>*Department of Astrophysical Sciences, Princeton University, 4 Ivy Lane, Princeton, NJ 08544, USA*

<sup>5</sup>*Space Telescope Science Institute, 3700 San Martin Drive, Baltimore, MD 21218, USA*

<sup>6</sup>*The Observatories of the Carnegie Institution for Science, 813 Santa Barbara St., Pasadena, CA 91101*

<sup>7</sup>*Mitchell Institute for Fundamental Physics and Astronomy and Department of Physics and Astronomy, Texas A&M University, College Station, TX 77843-4242, USA*

<sup>8</sup>*Institute of Astronomy, Madingley Rd, Cambridge CB3 0HA, UK*

<sup>9</sup>*Department of Physics and Kavli Institute for Astrophysics and Space Research, Massachusetts Institute of Technology, Cambridge, MA 02139, USA*

ABSTRACT

We report spectroscopic measurements of stars in the recently discovered young stellar association *Price-Whelan 1* (*PW 1*), which was found in the vicinity of the Leading Arm (LA) of the Magellanic Stream. We obtained Magellan+MIKE high-resolution spectra of the 28 brightest stars in *PW 1* and used The Cannon to determine their stellar parameters. We find that the mean metallicity of *PW 1* is  $[\text{Fe}/\text{H}] = -1.23$  with a small scatter of 0.06 dex and the mean radial velocity is  $V_{\text{hel}} = 276.7 \text{ km s}^{-1}$  with a dispersion of  $11.0 \text{ km s}^{-1}$ . Our results are consistent in  $T_{\text{eff}}$ ,  $\log g$ , and  $[\text{Fe}/\text{H}]$  with the young and metal-poor characteristics (116 Myr and  $[\text{Fe}/\text{H}] = -1.1$ ) determined for *PW 1* from our discovery paper. We find a strong correlation between the spatial pattern of the *PW 1* stars and the LA II gas with an offset of  $-10.15^\circ$  in  $L_{\text{MS}}$  and  $+1.55^\circ$  in  $B_{\text{MS}}$ . The similarity in metallicity, velocity, and spatial patterns indicates that *PW 1* likely originated in LA II. We find that the spatial and kinematic separation between LA II and *PW 1* can be explained by ram pressure from Milky Way gas. Using orbit integrations that account for the LMC and MW halo and outer disk gas, we constrain the halo gas density at the orbital pericenter of *PW 1* to be  $n_{\text{halo}}(17 \text{ kpc}) = 2.7_{-2.0}^{+3.4} \times 10^{-3} \text{ atoms cm}^{-3}$  and the disk gas density at the midplane at 20 kpc to be  $n_{\text{disk}}(20 \text{ kpc}, 0) = 6.0_{-2.0}^{+1.5} \times 10^{-2} \text{ atoms cm}^{-3}$ . We, therefore, conclude that *PW 1* formed from the LA II of the Magellanic Stream, making it a powerful constraint on the Milky Way–Magellanic interaction.

*Keywords:* Galaxy: open clusters and associations Galaxy: halo stars: formation surveys - Magellanic Clouds

1. INTRODUCTION

The gaseous Magellanic Stream (MS) and its Leading Arm (LA) component, which, respectively, trail and lead the Magellanic Clouds (MCs) in their orbit about the Milky Way (MW), are one of the most prominent

HI features in the sky (Wannier et al. 1972; Mathewson et al. 1974; Putman et al. 1998, 2003; Brüns et al. 2005; Nidever et al. 2008; Stanimirović et al. 2008). Together, the MS and LA stretch over  $200^\circ$  from end to end (Nidever et al. 2010), and are a prototypical example of a gaseous stream stripped from a satellite galaxy in the process of being accreted onto the MW.

The LA is composed of four main complexes (LA I–IV; Brüns et al. 2005; For et al. 2013), is shorter than the trailing stream, and has a more irregular shape, the latter two characteristics being likely due to

Corresponding author: David Nidever  
dnidever@montana.edu

\* Hubble Fellow  
Carnegie-Princeton Fellow

the effects of ram pressure. In fact, many of the LA cloudlets show head-tail shape (e.g., McClure-Griffiths et al. 2008). Two of the components, LA II and III, lie above the Galactic plane (i.e., at positive Galactic latitudes), suggesting that these complexes have already passed through the Galactic midplane. The formation of the LA has been a topic of great debate, but the proposed formation mechanisms have generally broken down into three primary physical processes: tidal stripping (e.g., Gardiner & Noguchi 1996; Connors et al. 2006; Besla et al. 2012; Diaz & Bekki 2012), ram pressure stripping (e.g., Mastropietro et al. 2005), and stellar feedback (e.g., Olano 2004; Nidever et al. 2008). Each formation mechanism has its own strengths and weaknesses in terms of explaining the LA morphology and kinematics. In the end, the formation of the LA is likely a combination of all three of these mechanisms, albeit their relative importance and chronological sequence remains an active topic of research (see the recent review by D’Onghia & Fox 2016).

With high-precision proper motion measurements of the MCs (e.g., Kallivayalil et al. 2006; Besla et al. 2007; Kallivayalil et al. 2013; Helmi et al. 2018), the first-infall scenario, e.g., that the MCs are on their first passage around the MW, has become a widely accepted model to explain both the dynamical evolution of the MCs and their interaction with the MW. In this scenario, the MCs were dynamically-bound long before they fell into the MW potential  $\sim 1$  Gyr ago (Besla et al. 2012). Many threads of observational evidence suggest that the MCs had the first strong gravitational interaction  $\sim 2$ – $3$  Gyr ago (e.g., Harris & Zaritsky 2004, 2009; Weisz et al. 2013) and then experienced a direct collision a few hundred Myr ago (e.g., Olsen et al. 2011; Besla et al. 2012; Noël et al. 2015; Choi et al. 2018a,b; Zivick et al. 2018). The majority of gas in the LA and MS was likely stripped during the former interaction, while the gas in the Magellanic Bridge was likely stripped off during the latter. However, the exact timing, mass, and origin (e.g., LMC or SMC) for the gas required to form the LA, MS, and the Magellanic Bridge remain unknown (Pardy et al. 2018).

Due to the differences in the star formation and baryon cycle histories of the LMC and SMC, the chemical abundances of the gas provide critical clues to understanding the origin and evolution of the Magellanic system. Abundances for high velocity clouds associated with the MS have been measured using absorption along the line-of-sight to a bright background source (a quasar or hot star), but appropriate sight lines are limited in number and location to produce a global characterization. A number of *HST* studies have found that the MS

has a mean metallicity of  $[\text{Fe}/\text{H}] \approx -1$  dex across its length (Fox et al. 2010, 2013b), although there is evidence for a more metal-rich component (Richter et al. 2013; Fox et al. 2013b). The Magellanic Bridge, the gas between the MCs, also has a metallicity of  $\approx -1$  (Lehner et al. 2008) as does the LA (Lu et al. 1998; Fox et al. 2018; Richter et al. 2018). The consistency in the metallicities for these distinct gaseous features that lead, trail, and connect the MCs suggests that they share a common originating system: the MCs, themselves. The current peak stellar metallicities of the LMC and SMC are  $[\text{Fe}/\text{H}] = -0.6$  dex and  $[\text{Fe}/\text{H}] = -1.0$  dex, and even higher in the innermost regions, which have ongoing star formation, reaching  $[\text{Fe}/\text{H}] = -0.2$  and  $[\text{Fe}/\text{H}] = -0.7$ , respectively (Nidever et al. 2019a). The current mean metallicity of the gas in the LMC and SMC is also high —  $[\text{Fe}/\text{H}] = -0.2$  and  $[\text{Fe}/\text{H}] = -0.6$ , respectively (Russell & Dopita 1992) — consistent with the most metal-rich stars. However, the gas components that formed the LA and MS were stripped some time ago and, therefore, their chemistry should be compared to the MCs in the past. According to Pagel & Tautvaišienė (1998); Harris & Zaritsky (2004) the MC metallicities were  $\sim 0.3$  dex lower  $\sim 2$  Gyr ago making the SMC’s metallicity consistent with those measured in the gaseous MS, LA, and Bridge today.

While the MCs are known to have extensive stellar peripheries (e.g., Muñoz et al. 2006; Majewski et al. 2009; Nidever et al. 2011, 2019b), no stars have been detected in the MS or LA despite many attempts (e.g., Philip 1976a,b; Recillas-Cruz 1982; Brueck & Hawkins 1983; Kunkel et al. 1997; Guhathakurta & Reitzel 1998). Recent star formation in the LA is expected because molecular hydrogen is ubiquitous in the LA (e.g., Richter et al. 2018) and shock compression caused by gas in both the Galactic disk and halo is anticipated. Indeed, Casetti-Dinescu et al. (2014) discovered a number of young stars in the region of the LA that had radial velocities consistent with being formed in the LA gas, initially confirmed by follow-up, high-resolution spectroscopy with Magellan+MIKE that enabled chemical abundance measurements of these stars. However, more recent high-resolution spectroscopy and orbital analyses incorporating Gaia DR2 (Brown et al. 2018) proper motions from the same team determined that the stars were incompatible with a Magellanic origin (Zhang et al. 2019).

While the initial claims of LA-associated young stars were invalidated with Gaia DR2 proper motions, Price-Whelan et al. (2018, hereafter Paper I) discovered a young stellar association (“Price-Whelan 1”; hereafter *PW 1*) using *Gaia* proper motions in the vicinity of the

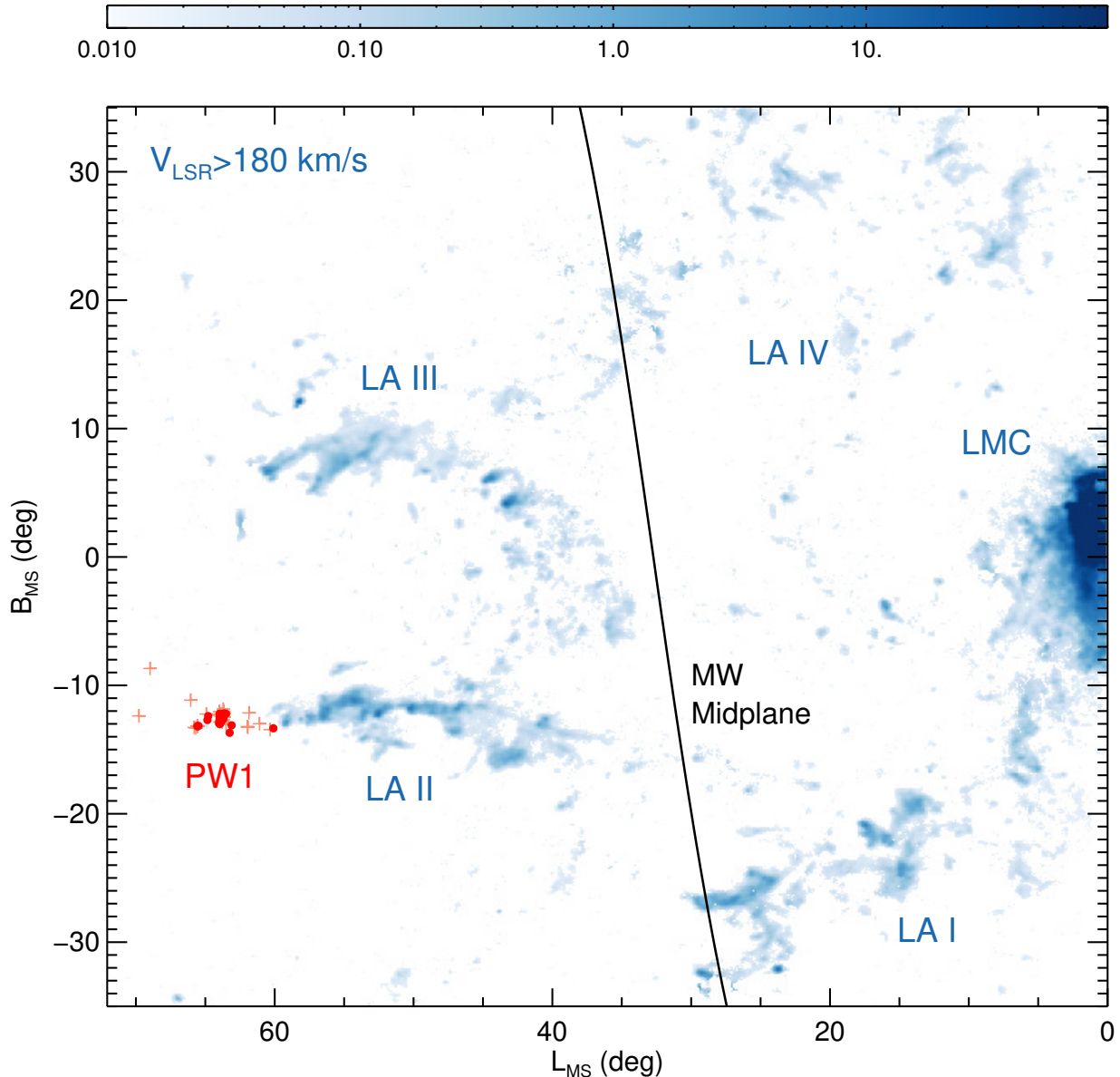


**Figure 1.** Map of the Leading Arm region. The GASS HI column density (in units of  $10^{19}$  atoms  $\text{cm}^{-2}$ ) is shown in blue with the LA I-IV and LMC labeled. The 28 PW1 stars for which we obtained MIKE spectra shown as filled red circles while the light-red crosses are 43 additional PW1 candidates based on photometry and Gaia DR2 proper motions. The MW midplane is shown by a solid black line.

LA. In [Paper I](#), *PW 1* was found to be young, metal-poor, and likely disrupting with a sky position similar to that of LA II. By comparing to stellar evolution models, [Paper I](#) measured an age of  $\sim 116$  Myr, distance of  $\sim 29$  kpc, metallicity of  $[\text{Fe}/\text{H}] = -1.14$ , and total present-day stellar mass of  $\sim 1200 M_{\odot}$ . Although the radial velocity (RV) of the cluster was unknown at the time, the range of possible orbits strongly suggested an association with the MCs and a passage through the outer MW disk  $\sim 116$  Myr ago. However, there are many

HI structures in the vicinity of *PW 1* (Figure 1), each with a unique RV signature. Associating *PW 1* with a particular gaseous substructure therefore requires spectroscopic RV measurements of the cluster stars.

In this paper, we analyze the stellar parameters and mean kinematics of the stars in *PW 1* to better constrain the properties and origin of this young stellar association. We also use the kinematics of *PW 1* in an orbital analysis to constrain the density of the MW hot halo and outer gas disk. The layout of the paper is as

follows: Section 2 describes the observations and data reduction. In Section 3, we present the procedures for deriving radial velocities and stellar parameters. Our main results are detailed in Section 4 and discussed in Section 5. Finally, our main conclusions are summarized in Section 6.

## 2. OBSERVATIONS AND REDUCTIONS

We obtained spectra for the brightest 28 *PW 1* stars and 6 standard stars using the Magellan Inamori Kyocera Echelle (MIKE) spectrograph (Bernstein et al. 2003) on Magellan-Clay at Las Campanas Observatory on 25, 26, and 30 April and May 1 2019. Some of the stars were also observed on 26, 27, 28 December 2018 using the Goodman Spectrograph (Clemens et al. 2004) at the SOAR Telescope with consistent results. Table 1 presents the names, coordinates, magnitudes, signal-to-noise ratio (S/N) and proper motions for each target. Figure 2 shows their location in a *Gaia* color-magnitude diagram (red open circles) relative to all *PW 1* candidates (blue) and field stars (black). Observations were taken with the  $0.7''$  slit and  $2 \times 2$  pixel binning, such that the native resolution for each spectrum is  $R = 31,000$ . Exposure times ranged from 70 to 1060 seconds under generally good conditions with an average seeing of  $0.7''$ . At the native MIKE resolution, S/N per resolution element (3.15 pixels) for the *PW 1* stars is 10–24 with a median of  $\sim 18$ , although the S/N per pixel is increased by  $3.16 \times$  by rebinning the 1-D extracted spectra (see below). Six of the stars have low S/N due to moderately cloudy conditions (PW1-00 – PW1-05) and are generally excluded from detailed analysis. An additional high-S/N spectrum was obtained for PW1-00 (the brightest *PW 1* member) that is suitable for precise chemical abundance work, but this analysis is reserved for future work.

The observations were processed using the MIKE pipeline<sup>1</sup>, which is part of the CarPy spectroscopic reduction package that uses algorithms described in Kelson et al. (2000) and Kelson (2003). The MIKE pipeline performs image processing (bias removal, flat fielding) as well as extracting the spectra, determining a wavelength solution, subtracting the sky, and co-adding multiple exposures of single objects. The multi order reduced spectra were then merged into a single spectrum and normalized using the IRAF<sup>2</sup> tasks `continuum` and

<sup>1</sup> Available: <https://code.obs.carnegiescience.edu/mike>

<sup>2</sup> IRAF is distributed by the National Optical Astronomy Observatories, which are operated by the Association of Universities for Research in Astronomy, Inc., under cooperative agreement with the National Science Foundation.

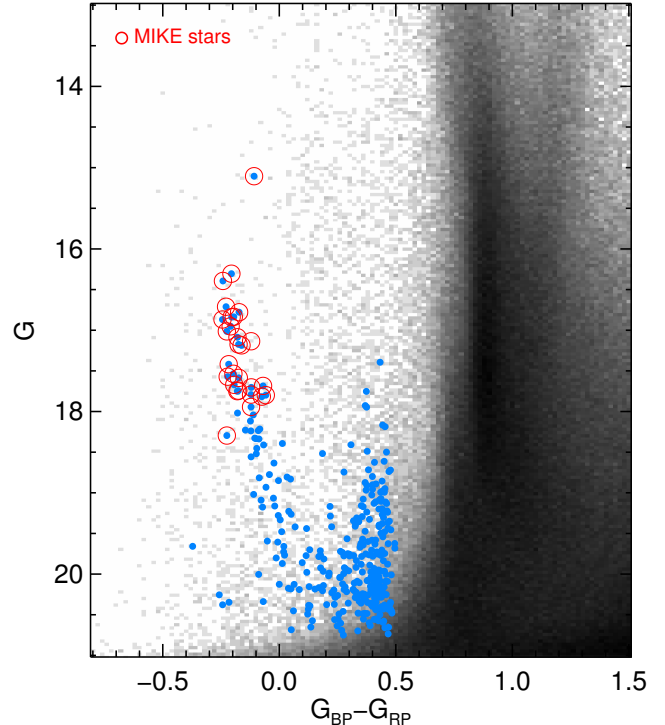


**Figure 2.** Color-magnitude diagram using *Gaia* photometry in the vicinity of *PW 1* (black points); the specific spatial constraints are  $173.5^\circ < \alpha < 185.5^\circ$ ,  $-35.0^\circ < \delta < -23.0^\circ$ . Filled (blue) circles are probable *PW 1* members (with  $G_{BP} - G_{RP} < 0.5$ ) based on the proper motion model described in Paper I. MIKE spectra were obtained for the 28 stars indicated by open red circles, including PW1-03 which was not used in the analysis due to low S/N.

`scombine`. While MIKE produces spectra from the blue and red arms, only blue spectra with a wavelength range of 3550–5060Å were used in our analysis. Figure 3 shows example spectra for two *PW 1* stars and the standard star HD 146775.

Finally, the full MIKE resolution was significantly higher than needed for our science goals. Therefore, we rebinned the spectra with a bin size of 10 native MIKE pixels which increased the S/N per pixel by  $\sim 3.16 \times$ . This had little impact on the spectral features as they are already quite broad in these hot, B-type stars.

## 3. DATA ANALYSIS

### 3.1. Radial Velocities

A RV was determined for each star via a two phase process. First, we determine an initial RV for each source by cross-correlating the unsmoothed MIKE spectra (excluding the region below 3665Å) with a hot synthetic stellar spectrum having stellar parameters ( $T_{\text{eff}}$ ,  $\log g$ ,  $[\text{Fe}/\text{H}]$ ) = (15,000K, 4.0,  $-1.0$ ) and set to the the resolution and logarithmic wavelength scale of the MIKE

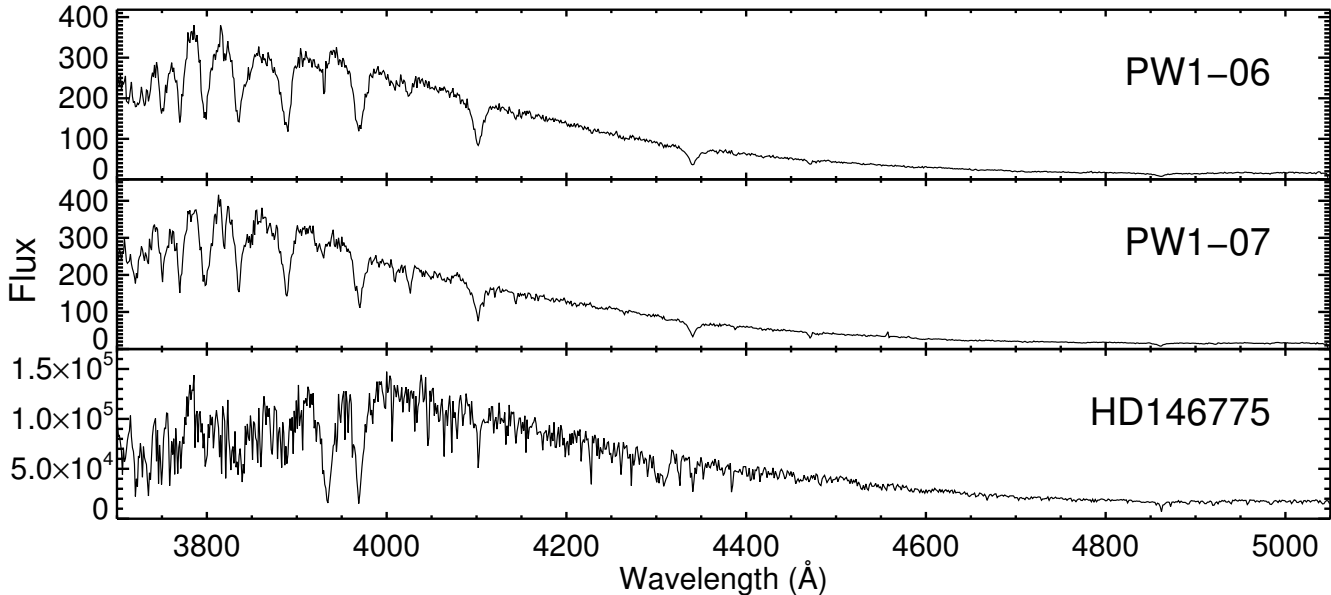


**Figure 3.** Three example MIKE blue-arm spectra. The top two panels show example *PW 1* stars, PW1-06 (s/N=29) and PW1-07 (S/N=30), while the bottom panel is the reference star HD146775 (S/N=826).

spectra. Second, the RVs were then redetermined using its best-fit model as the cross-correlation template after the star-by-star stellar parameters were determined following the procedure described in §3.2. The second iteration provided similar, but more precise and accurate RV solutions.

We determine the RV uncertainties using a Monte Carlo scheme. Mock observations were generated for each star by adding Gaussian noise similar to that observed in the science spectrum to its best-fit model spectrum. One hundred mock observations were generated for each star, the RV determined for each with the method described above, and the uncertainty calculated as the robust standard deviation of these values. The typical RV uncertainty from this procedure is  $\sim 3$  km s $^{-1}$  but the uncertainty increases roughly with the inverse of S/N.

We compared our RVs for the six bright standard stars to literature values and find a median offset of  $-2.0$  km s $^{-1}$ , which is consistent within the uncertainties of our measurements.

### 3.2. Stellar Parameters

We use *The Cannon*<sup>3</sup> (Casey et al. 2016; Ness et al. 2015) to determine stellar parameters ( $T_{\text{eff}}$ ,  $\log g$ , [Fe/H]) for our 28 spectra. The Cannon is a data-driven model for stellar spectra in which the stellar flux (at a given wavelength) is parameterized as a polynomial function of stellar parameters and abundances (i.e., “la-

bels”). A Cannon “model” is trained on a set of spectra (observed or synthetic) with well-known labels (i.e., the “training set”) and can then be used to determine the labels for other spectra. An advantage of this method is that it exploits all the information available in the spectra and is also fully automated. First, we construct a grid of 330 synthetic spectra (at a resolution of  $1.5\text{\AA}$ ) with the Synspec<sup>4</sup> (Hubeny & Lanz 2011, 2017) spectral synthesis software and IDL wrappers and auxiliary scripts (Allende Prieto, private communication). Given an input atmospheric model, a linelist and stellar parameters and abundances, Synspec solves the radiative transfer equation over a specified wavelength range and resolution resulting in a synthetic spectrum. We use the Kurucz LTE atmospheric models and include both atomic and molecular lines. For the spectral grid, the  $T_{\text{eff}}$  ranges from 11,000K to 21,000K in steps of 1,000K, the  $\log g$  ranges from 2.0 to 5.0 in steps of 0.5 dex, and the [Fe/H] ranges from  $-1.5$  to  $+0.5$  in steps of 0.25 dex (the boundary of the grid is shown in the bottom panel of Figure 6). The synthetic spectra were interpolated onto the wavelength grid of the final MIKE spectra and normalized. For *The Cannon* model, we used a quadratic polynomial model to represent how the flux varies with the three stellar parameters at each wavelength. To provide a simple sanity check of the model generated by *The Cannon*, we determined the stellar parameters for the training set spectra using *The Cannon* model and compared these results to the training

<sup>3</sup> <https://github.com/andycasey/AnniesLasso>

<sup>4</sup> <http://nova.astro.umd.edu/Synspec43/synspec.html>

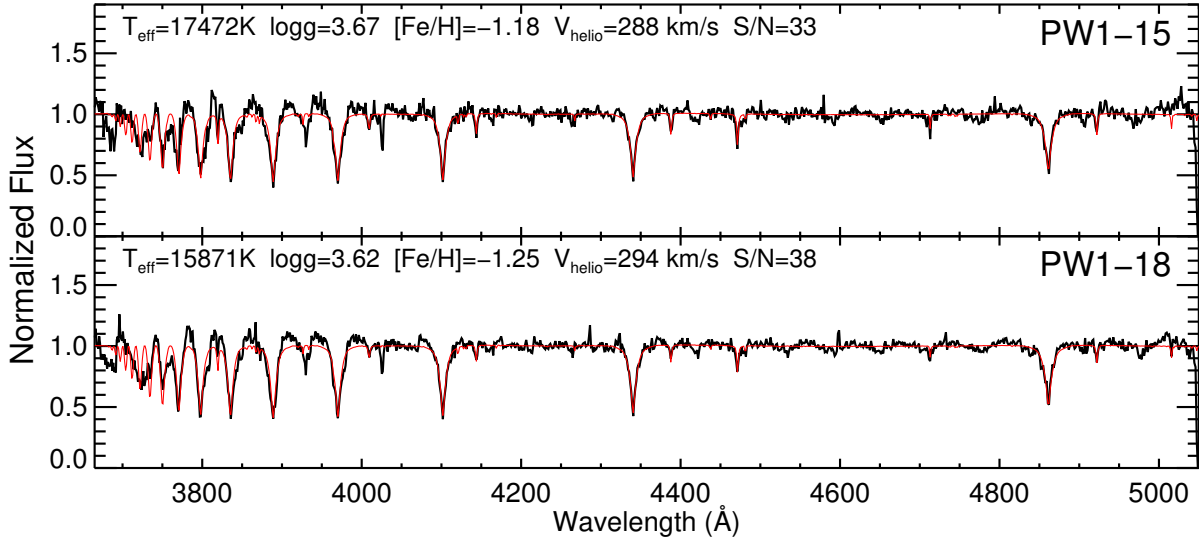


**Figure 4.** Example best-fit spectra from *The Cannon*. MIKE spectra for PW1-15 and PW1-18 (black) are shown with the best-fit Cannon models overlaid (red). These show excellent agreement. The best-fit stellar and RV parameters are noted in the top left corner for each star.

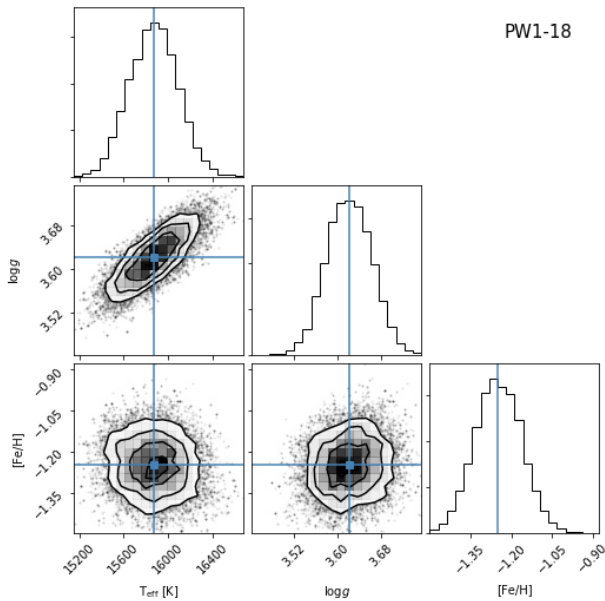


**Figure 5.** An example corner plot showing the *emcee* MCMC posterior distributions for PW1-18. The median values are shown by the blue lines.

set input parameters. We found no significant biases. Specifically, the  $T_{\text{eff}}$  had an offset of 0.5K and scatter of  $\sigma=250\text{K}$ ,  $\log g$  had a mean offset of  $-0.003$  dex and  $\sigma=0.06$  dex, while  $[\text{Fe}/\text{H}]$  had no offset with a scatter of  $\sigma=0.12$  dex.

We use the initial stellar parameters determined with *The Cannon* to refine the normalization of the MIKE

spectra using a scaling factor determined by the ratio of the observed spectrum divided by the best-fit Cannon spectrum with heavy Gaussian-smoothing ( $\text{FWHM} = 38\text{\AA}$ ). New *Cannon* solutions were then found for these “renormalized” observed spectra. Two example fits from *The Cannon* are shown in Figure 4 in comparison to their best-fit *Cannon* model and its parameters.

We use the *emcee* (Foreman-Mackey et al. 2013; Goodman & Weare 2010) MCMC sampler to determine the stellar parameters for each star and their uncertainties. We run with 30 walkers for 1000 step and the first 200 are discarded as “burn-in” steps. Figure 5 shows an example “corner” plot of the posterior distributions for PW1-18 and the median values with the blue lines. Typical statistical uncertainties are  $\sim 300\text{K}$  in  $T_{\text{eff}}$ , 0.06 dex in  $\log g$ , and 0.10 dex in  $[\text{Fe}/\text{H}]$ .

Figure 6 shows the distribution of  $\log g$  vs.  $T_{\text{eff}}$  color-coded by  $[\text{Fe}/\text{H}]$  and  $V_{\text{LSR}}$  in comparison to PARSEC isochrones. We note that one or two stars (including PW1-13) might be hot horizontal branch (HB) stars based on the best-fit  $\log g$  and  $T_{\text{eff}}$  (e.g., Zhang et al. 2019). Confirming whether a star is either on the HB or MS evolutionary stage is beyond the scope of this paper due to the lack of He abundance information. However, we emphasize that inclusion of a few potential HB stars does not affect our dynamical analysis and main conclusions because all the stars in our sample share consistent proper motions and radial velocities.

Figure 7 shows the resulting  $[\text{Fe}/\text{H}]$  distribution of *PW 1* stars, which is peaked at  $[\text{Fe}/\text{H}] \approx -1.23$  and has a dispersion of 0.06 dex. This spectroscopically-measured

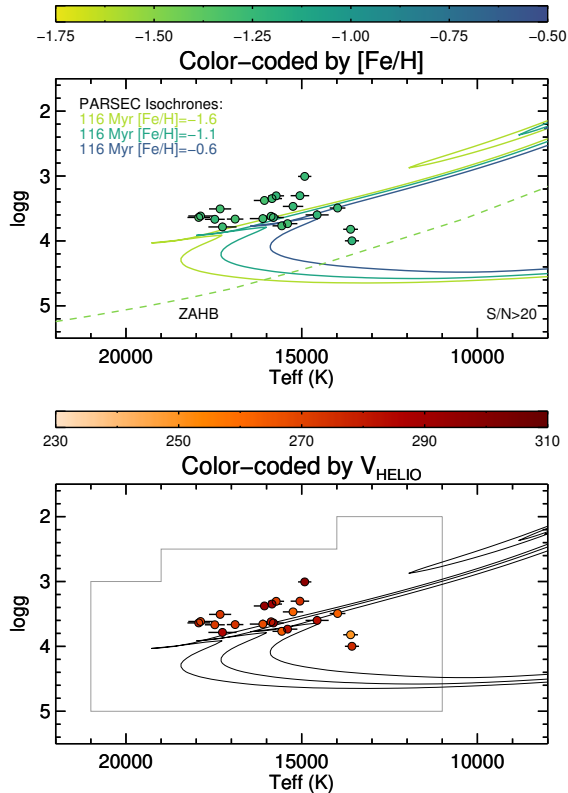


**Figure 6.** Stellar parameters determined from *The Cannon* for the 21 *PW 1* stars with  $S/N \geq 20$  and compared to PARSEC isochrones. The top panel shows  $\log g$  vs.  $T_{\text{eff}}$  color-coded by  $[\text{Fe}/\text{H}]$  whereas the bottom shows the same points color-coded by  $V_{\text{helio}}$ . As indicated by color coding in the top panel, the isochrones have an age of 116 Myr and a metallicity of  $[\text{Fe}/\text{H}] = -1.6, -1.1$  and  $-0.6$  dex, respectively. The  $[\text{Fe}/\text{H}] = -1.48$  Zero-Age Horizontal Branch (ZAHB) from Dorman et al. (1993) is also shown as a dashed line. The boundary of the synthetic spectral grid used in *The Cannon* analysis is shown in light gray in the bottom panel.

metallicity is in good agreement with our photometry-based metallicity measurement of  $[\text{Fe}/\text{H}] = -1.1$  in Paper I. The small dispersion of the *PW 1*  $[\text{Fe}/\text{H}]$  values suggests that our uncertainties might be overestimated and that our true uncertainties are closer to  $\sim 0.05$  dex. The derived stellar parameters and their uncertainties are also provided in Table 1.

## 4. RESULTS

### 4.1. *PW 1* Velocity

With proper motion and radial velocity information for individual stars in *PW 1*, along with a constraint on the mean distance to *PW 1* (Paper I), we construct a simple model for its internal velocity structure to infer the true mean velocity and velocity dispersion from

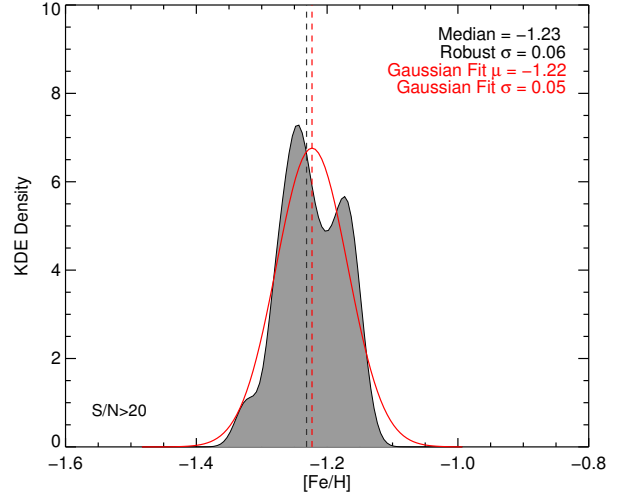


**Figure 7.** Kernel Density Estimate (KDE) of the distribution of  $[\text{Fe}/\text{H}]$  measurements for 21 *PW 1* stars with  $S/N \geq 20$  and a bandwidth of 0.04 dex, which is smaller than the typical  $[\text{Fe}/\text{H}]$  uncertainty of  $\sim 0.10$  dex. A single Gaussian model is fit to the histogram and has peak at  $-1.22$  and  $\sigma$  of 0.05 dex. The median  $[\text{Fe}/\text{H}]$  is  $-1.23$ , the standard deviation is 0.06 dex.

these projected quantities. We use the  $N = 22$  (out of 28) stars with spectroscopic  $S/N \geq 10$  for this analysis.

We assume that the 3-D velocity of each  $n$  star,  $\mathbf{v}_n$ , is drawn from a 3D Gaussian with mean  $\mathbf{v}_0$  and a diagonal covariance matrix  $\mathbf{C} = \sigma_v^2 \mathbb{I}_3$ , where  $\sigma_v$  is the (assumed isotropic) velocity dispersion, and  $\mathbb{I}_3$  is the identity matrix.<sup>5</sup> For each individual star, we only observe projected or astrometric quantities, like sky position  $(\alpha, \delta)$ , distance  $d$ , proper motions  $(\mu_\alpha, \mu_\delta)$ , and radial velocity  $v_r$ . We assume that the sky position of each star is known with infinite precision, the observed distance is unresolved and given by the mean cluster distance and uncertainty (Paper I), the proper motions are given by *Gaia* with a 2D covariance matrix  $\mathbf{C}_\mu$ , and the radial velocities are measured in this work. The (unobserved) true 3D velocity of each star, drawn from the model given above, is related to the observed astrometric quantities through a projection matrix that depends on sky position (see, e.g., the appendix of Oh et al. 2017). The full model therefore has  $N + 3N + 3 + 1 = 92$  parameters: the true distance to each star, the true 3D velocity vector of each star, the mean velocity of *PW 1*, and the velocity dispersion. This model is implemented in the *Stan* (Car-

<sup>5</sup> We also tried allowing generic velocity anisotropies (non-diagonal  $\mathbf{C}$ ) but found that the resulting matrix was consistent with being isotropic within the derived uncertainties.

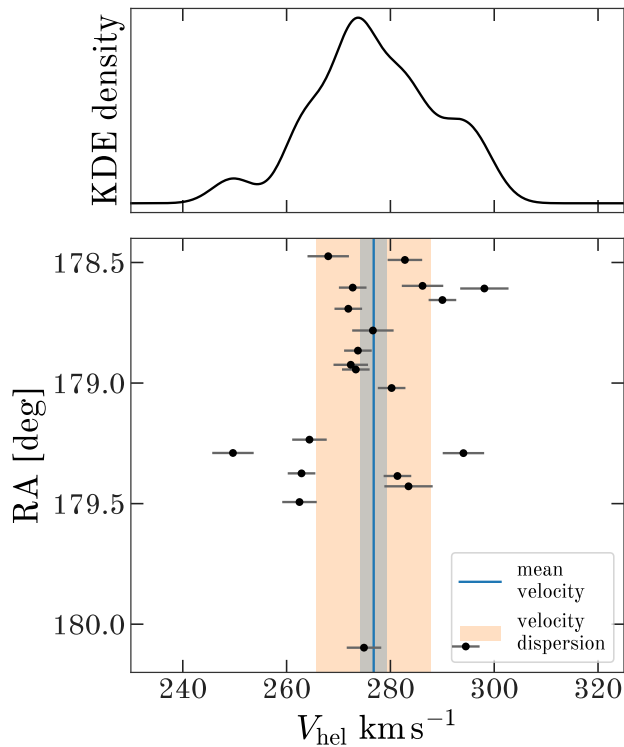


**Figure 8.** *Top panel:* Kernel density estimate of the distribution of RV measurements with a bandwidth  $b = 3 \text{ km s}^{-1}$ . *Bottom panel:* Individual RV measurements for *PW 1* stars with uncertainties (black markers and error bars) as a function of right ascension (RA). The solid line (blue) shows the inferred mean RV of *PW 1*, and the shaded (blue) region shows the uncertainty on the mean RV,  $276.7 \pm 2.5 \text{ km s}^{-1}$ . The larger shaded region (orange) shows the median posterior value of the velocity dispersion of *PW 1*,  $11.0 \pm 2 \text{ km s}^{-1}$ .

penter et al. 2017) probabilistic programming language, and we use the built-in No-U-Turn Hamiltonian Monte Carlo sampler (Homan & Gelman 2014) to generate posterior samples over all of the model parameters. We run the sampler for 4000 steps in total for 4 independent Markov Chains: 2000 burn-in and tuning steps (that are discarded), and then a further 2000 steps for each chain, from which we assess convergence by computing the effective sample size and Gelman-Rubin convergence statistic for each chain.

Given the posterior samples generated as described above, we measure a mean barycentric radial velocity for *PW 1* of  $276.7 \pm 2.5 \text{ km s}^{-1}$  and mean proper motion of  $(-0.52, 0.42) \pm (0.04, 0.03) \text{ mas yr}^{-1}$ . Assuming a total solar velocity of  $(11.1, 220 + 12.24, 7.25) \text{ km s}^{-1}$  (Schönrich et al. 2010), this corresponds to a Galactocentric (Cartesian) velocity for *PW 1* of  $v_{\text{galcen}} \approx (0.6, 2.2, 186) \text{ km s}^{-1}$ . We find a velocity dispersion of  $\sigma_v = 11.0 \pm 2 \text{ km s}^{-1}$ , which is consistent with a robust standard deviation computed from the RVs alone (§3.1),

indicating that the constraint on the velocity dispersion comes predominantly from the RV data in this work. Figure 8 shows the individual RV measurements of each observed *PW 1* star (black points) as a function of right ascension, along with the inferred mean velocity (blue) and velocity dispersion (orange).

In the sections to follow, we compare the inferred line-of-sight velocity of *PW 1* with HI radio data (e.g., from GASS) where it is necessary to convert to the “kinematic local standard of rest” (LSRK), which historically uses the average of Solar neighborhood star velocities (Delhaye 1965; Gordon 1976)<sup>6</sup>. In this reference frame, the mean velocity is  $V_{\text{LSR}} = 273.4 \pm 2.5 \text{ km s}^{-1}$ .

#### 4.2. Leading Arm Origin

Figure 9 shows the position–velocity diagram of the *PW 1* stars and the HI gas (GASS; McClure-Griffiths et al. 2009) using the Gaussian decomposition techniques described in Nidever et al. (2008). The mean  $V_{\text{LSR}}$  velocity of  $273.4 \text{ km s}^{-1}$  of the *PW 1* stars is very similar to the velocity of the LA II gas of  $233 \text{ km s}^{-1}$ . Absorption-line studies of the LA HI find a value of  $[\text{Fe}/\text{H}] \sim -1$  dex (Lu et al. 1998; Fox et al. 2018; Richter et al. 2018), which is similar to the mean metallicity of *PW 1* stars studied here of  $[\text{Fe}/\text{H}] \sim -1.23$  dex (see Figure 7). Therefore, we conclude that the *PW 1* stars are physically associated with the LA II gas based on their similar RVs and metallicities.

#### 4.3. Spatial Offset between Stars and Gas

The current location of *PW 1* is close to LA II on the sky, but there is little gas in its immediate vicinity in the position-velocity diagram (Figure 9). The top panel of Figure 10 shows the spatial offset between *PW 1* and the LA II gas in the MS coordinate system ( $L_{\text{MS}}, B_{\text{MS}}$ ). The gas from which *PW 1* originated should experience ram pressure from the MW hot halo gas (e.g., Mastropietro et al. 2005). Because the stars will not feel this force, the gas and stars will decouple over time with the net effect that the gas trails the stars in their orbit. With this in mind, it is not surprising that there is little gas in the immediate vicinity of *PW 1*. Thus, the spatial offset does not rule out LA II as the origin gas for *PW 1*.

Quantitatively, the magnitude of the spatial decoupling between the stars and gas is determined by a 2D cross-correlation of the star and gas maps (Figure 10, top). The individual maps were masked such that only the highest density regions were used. The result of the cross-correlation is in the middle panel of

<sup>6</sup> The solar motion is assumed to be  $20.0 \text{ km s}^{-1}$  towards  $(18\text{h}, +30^\circ)$  at epoch 1900.0.

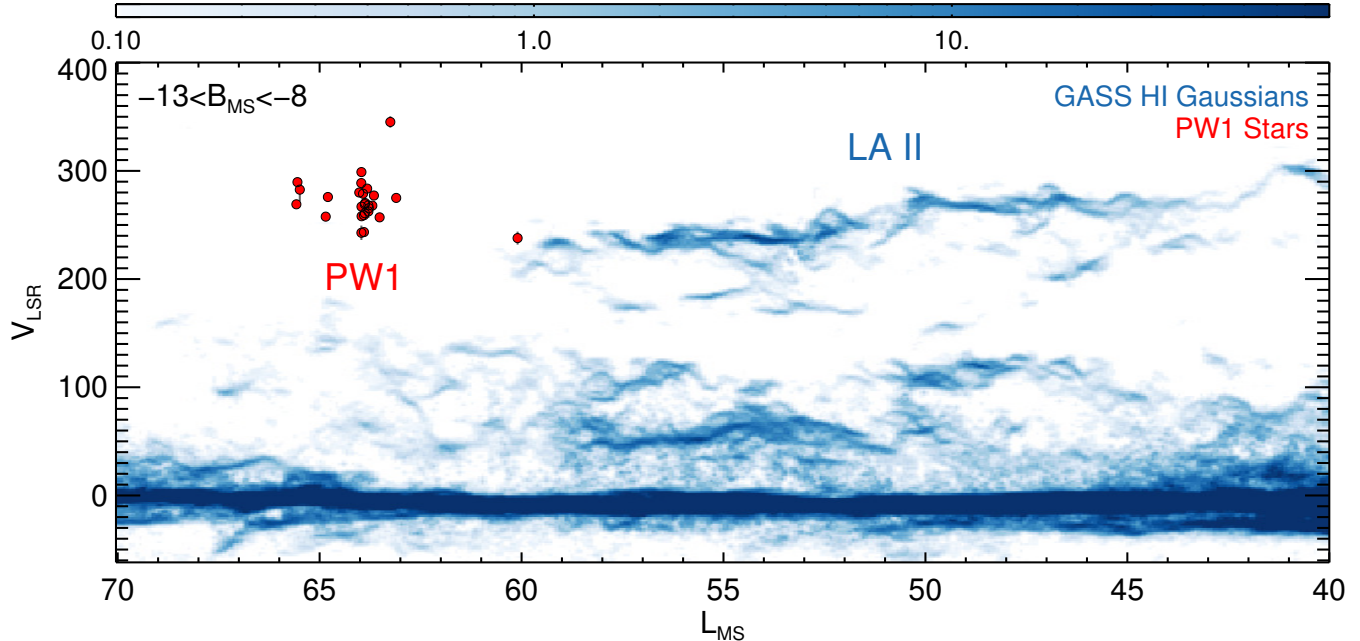


**Figure 9.** Position–velocity diagram of the *PW 1* stars compared to the GASS HI data (McClure-Griffiths et al. 2009). The background bluescale image is the integrated intensity of the GASS Gaussian centers summed along  $B_{\text{MS}}$  in units of  $10^{18}$  atoms  $\text{cm}^{-2}$  degree. The tip of LA II has a velocity of  $\sim 233$   $\text{km s}^{-1}$ . Each *PW 1* star is plotted at its determined  $V_{\text{LSR}}$  as a red filled circle with its uncertainty. The stars have a mean velocity of  $\sim 273.4$   $\text{km s}^{-1}$ , slightly higher than but similar to the gas in LA II.

**Figure 10.** The peak of the cross-correlation is at an offset of  $(-10.15^\circ, +1.44^\circ)$  in  $(L_{\text{MS}}, B_{\text{MS}})$ , which is indicated as a red cross in the middle panel of **Figure 10**. The bottom panel of **Figure 10** shows that shifted *PW 1* positions are well aligned with the high-density peaks of the HI gas. These shift positions are more representative of the original relative positioning of the gas forming *PW 1* within the LA II complex.

**Figure 11** shows a slightly different visualization of this process. The top panel of **Figure 11** zooms into the  $(L_{\text{MS}}, B_{\text{MS}})$  region around the position-shifted stars with  $V_{\text{LSR}}$  measurements. Ram pressure will also act to modify the velocities of the gas it acts on, and thus an exact match between the velocities of the birth-gas and resulting stars is not expected. The bottom panel of **Figure 11** is the resulting velocity-position diagram; a  $30$   $\text{km s}^{-1}$  velocity offset is required to have the *PW 1* stars align with the densest portions of the gas in position-velocity space. We will use this offset in the next section to place a constraint on the halo gas driving the ram pressure effects.

#### 4.4. Ram Pressure

If the spatial and velocity offsets between this gas and *PW 1* are indeed due to a roughly constant ram pressure, then the measured position-velocity offsets become a means of inferring the properties of the gas performing

the ram pressure. In particular, we place a constraint on the average density of the “hot” MW-halo gas, a medium that remains difficult to characterize directly (for an overview see Putman et al. 2012).

At a distance of 29 kpc, the angular offset of  $10.15^\circ$  corresponds to a tangential distance of  $\sim 5.14$  kpc. Over 116 Myr that corresponds to a mean “drift” velocity of  $\sim 43.3$   $\text{km s}^{-1}$  or a deceleration of  $\sim 0.747$   $\text{km s}^{-1} \text{Myr}^{-1}$ . The total change in the tangential velocity of the gas over this period is  $\sim 86.6$   $\text{km s}^{-1}$ . The  $V_{\text{LSR}}$  of LA II “tip” is lower than that of *PW 1* by  $\sim 30$   $\text{km s}^{-1}$ . The smaller  $V_{\text{LSR}}$  shift would indicate that a significant fraction of the deceleration occurred in the tangential direction.

If we assume that ram pressure is the main factor in causing the gas and stars to drift apart and that this is dominated by a roughly constant ram pressure from the MW hot halo, then we can estimate the density of the MW hot halo gas as follows. The ram pressure experienced by the *PW 1* “birth cloud” (BC) in LA II is defined as,

$$P = \rho_{\text{MW}} v_{\text{BC}}^2, \quad (1)$$

where  $\rho_{\text{MW}}$  is the density of the MW halo gas and  $v_{\text{BC}}$  is the birth cloud velocity through the medium. If  $l_{\text{BC}}$  is the approximate diameter of the birth cloud, then the

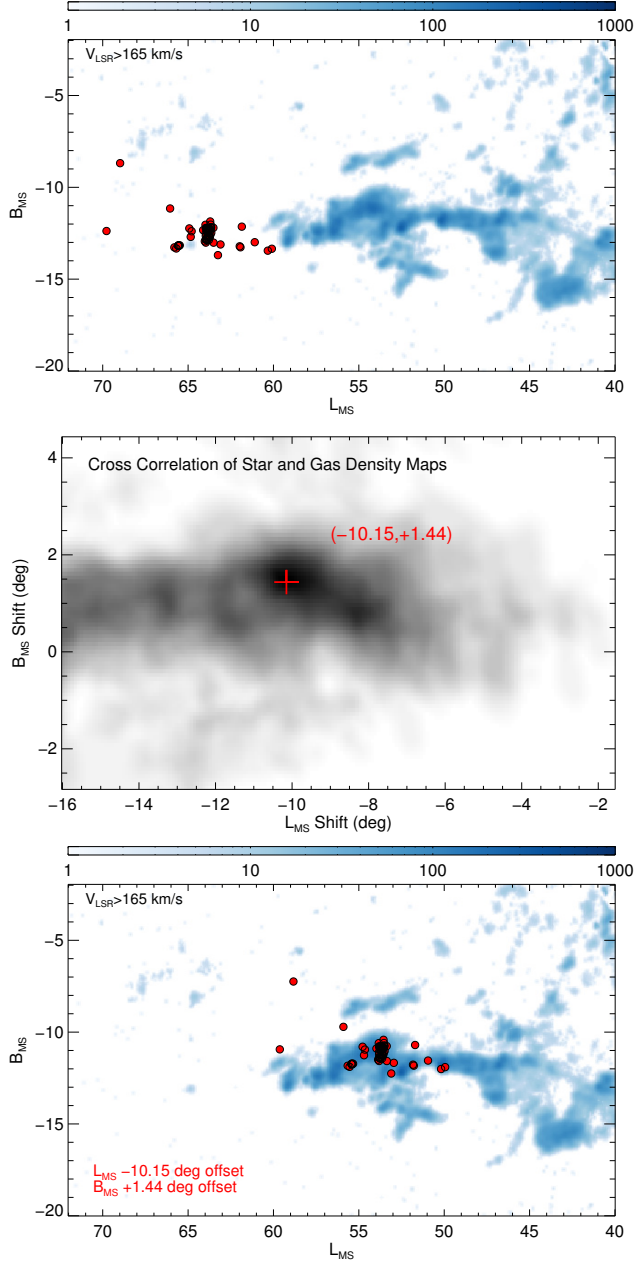


**Figure 10.** The spatial distribution of the HI gas and 71 *PW 1* candidate stars based on photometry and Gaia DR2 proper motions. (top) The gas and *PW 1* stars at their current ( $L_{\text{MS}}, B_{\text{MS}}$ ) positions. (middle) The 2D cross-correlation map of the star and gas density maps with the shift of  $(-10.15^\circ, +1.44^\circ)$  in  $(L_{\text{MS}}, B_{\text{MS}})$ . (Bottom) *PW 1* shifted by the offset determined in the cross-correlation.

acceleration that it experiences ( $a_{\text{BC}}$ ) is,

$$a_{\text{BC}} \approx \frac{\rho_{\text{MW}} v_{\text{BC}}^2 l_{\text{BC}}^2}{\rho_{\text{BC}} l_{\text{BC}}^3} \approx \frac{\rho_{\text{MW}} v_{\text{BC}}^2}{\rho_{\text{BC}} l_{\text{BC}}}. \quad (2)$$

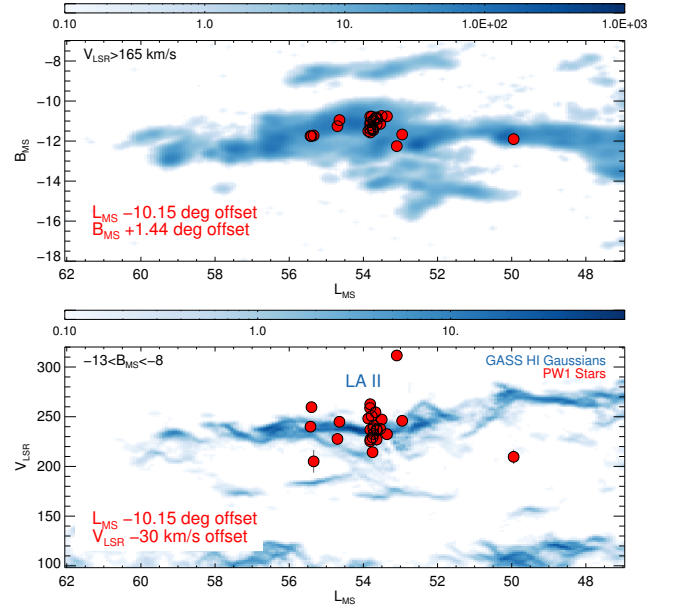


**Figure 11.** Spatial and Position–velocity diagram for the 28 *PW 1* stars with radial velocities and LA II gas. The top panel shows the positions of the *PW 1* stars (red filled circles) and the LA II gas after the cross-correlation offset has been applied (see Figure 10). The bottom panel shows the same spatially-offset stars in position-velocity space. A  $V_{\text{LSR}}$  offset of  $30 \text{ km s}^{-1}$  has been applied such that the stars align with the densest portions of the LA II gas.

Solving Equation 2 for the ratio of gas density between the MW and the birth cloud gives

$$\frac{\rho_{\text{MW}}}{\rho_{\text{BC}}} \approx \frac{a_{\text{BC}} l_{\text{BC}}}{v_{\text{BC}}^2}. \quad (3)$$

If we assume that the birth cloud was undergoing a roughly constant deceleration due to ram pressure since forming *PW 1*, then we can estimate this deceleration from the age of *PW 1* ( $\Delta t = 116 \text{ Myr}$ ) and the spatial offset ( $\Delta x = 10.15^\circ = 5.14 \text{ kpc}$ ), as

$$a_{\text{BC}} \approx \frac{2\Delta x}{\Delta t^2}. \quad (4)$$

This results in  $a_{\text{BC}} \approx 0.747 \text{ km s}^{-1} \text{ Myr}^{-1}$ . The angular width (full-width at half-maximum in  $B_{\text{MS}}$ ) of the LA II *PW 1* birth cloud from GASS is  $0.75^\circ$  or  $0.38 \text{ kpc}$ . Using this as an approximation of the diameter of the birth cloud ( $l_{\text{BC}}$ ) and  $v_{\text{BC}} \approx 235 \text{ km s}^{-1}$ , we obtain  $\rho_{\text{MW}}/\rho_{\text{BC}} \approx 0.00505$  or that the MW gas density is  $\sim 0.5\%$  of that of the *PW 1* birth cloud.

We measure the average current column density of the *PW 1* birth cloud from the HI GASS data as  $N_{\text{HI}} \approx 1.5 \times 10^{20} \text{ atoms cm}^{-2}$ . Assuming a distance of  $29 \text{ kpc}$  and a width of  $\sim 0.38 \text{ kpc}$  gives a number density of  $n_{\text{BC}} \approx 0.128 \text{ atoms cm}^{-3}$ .

Finally, we derive the number density of the hot MW halo as  $n_{\text{MW}} \approx 6.46 \times 10^{-4}$  atoms  $\text{cm}^{-3}$ . This rough estimate of the hot MW halo gas density is an order of magnitude higher than that predicted by the Miller & Bregman (2013) model which gives  $\sim 4 \times 10^{-5}$  atoms  $\text{cm}^{-3}$  at this location. However, our estimate here is too simplistic for a number of reasons: (i) we are seeing an integrated effect over the orbit of *PW 1*, which has passed through higher densities closer to the midplane, and (ii) we consider only a single medium – the hot halo – completely ignoring the impact of the midplane and outer gas disk itself. That this simple estimate is within an order-of-magnitude of state-of-the-art measurements motivates the more complex and nuanced simulations that are presented in the next sub-section.

#### 4.5. Ram pressure orbit analysis

The offsets in sky position and velocity between the *PW 1* stars and the LA II gas suggest that the gas was likely subject to a drag force or dissipated orbital energy: The offset in position is primarily along the direction of motion, and the gas velocity is slightly lower than that of *PW 1*. Moreover, the order-of-magnitude computations presented in the previous sub-section suggest that ram pressure from the hot halo produce effects on par with what is seen, albeit more complex interactions of the mid-plane are ignored. We therefore perform a set of orbit integrations to see if the observed position-velocity offsets can plausibly be explained by gas drag from the MW halo when the full orbital motion and influence of the midplane are included.

We use the MW mass model implemented in *gala* (Bovy 2015; Price-Whelan 2017) as the background gravitational potential, and include a time-dependent mass component to represent the LMC. In detail, we represent the mass distribution of the LMC using a Hernquist profile (Hernquist 1990), which generally follows the the approach used in Erkal et al. (2019), except that we use a total mass of  $M_{\text{LMC}} = 2.5 \times 10^{11} M_{\odot}$  (Laporte et al. 2018). We compute the position of the LMC at any given time by integrating the orbit of the LMC center-of-mass backwards from its present day phase-space position (using initial conditions from Patel et al. 2017). We neglect any back-reaction or response of the MW to the presence of the LMC. We use this time-dependent mass model along with the measured position and velocity of *PW 1* to numerically integrate the orbit of the *PW 1* backwards in time from present day ( $t_2 = 0$ ) to its birth time ( $t_1 = -\tau = -116$  Myr). We use the Dormand-Prince 8th-order Runge-Kutta scheme (Dormand & Prince 1980) to numerically integrate these orbits.

Once the phase-space coordinates of *PW 1* at its birth time are estimated, we then integrate forward in time, now including the effects of gas drag and momentum coupling between the MW disk and the LA II gas as it crosses the Galactic midplane. We compute the drag acceleration on the gas as

$$\mathbf{a}_{\text{drag}} = n_{\text{MW}}(\mathbf{x}) |\mathbf{v}|^2 \Sigma_{\text{LA}}^{-1} \times -\frac{\mathbf{v}}{|\mathbf{v}|} \quad (5)$$

where  $n_{\text{MW}}(\mathbf{x})$  is the number density of MW gas at position  $\mathbf{x}$ ,  $\mathbf{v}$  is the orbital velocity, and  $\Sigma_{\text{LA}}$  is the surface density of the LA gas (following, e.g., Vollmer et al. 2001). For the gas density, we use the gaseous halo model from Miller & Bregman (2013) and the disk model from Kalberla & Kerp (2009) with a Gaussian density profile in the height above the midplane  $z$  such that

$$n_{\text{MW}}(\mathbf{x}) = n_{\text{halo}}(r) + n_{\text{disk}}(R, z) \quad (6)$$

$$n_{\text{halo}}(r) = n_{0,h} \left[ 1 + \left( \frac{r}{r_c} \right)^2 \right]^{-3\beta/2} \quad (7)$$

$$n_{\text{disk}}(R, z) = n_{0,d} e^{-\frac{R-R_{\odot}}{R_n}} e^{-\frac{1}{2} \frac{z^2}{\sigma_z(R)^2}} \quad (8)$$

$$\sigma_z(R) = 0.85 h_0 e^{\frac{R-R_{\odot}}{R_0}} \quad (9)$$

where  $r$  is the spherical radius,  $R$  is the cylindrical radius,  $R_{\odot} = 8.1$  kpc is the solar Galactocentric radius, and all parameter values are taken from Kalberla & Kerp (2009). We assume that the surface density of the *PW 1* birth cloud in LA II starts with  $\Sigma_0 \approx 50 M_{\odot} \text{pc}^{-2}$  (comparable to other LMC molecular clouds Wong et al. 2011) and ends (at present day) with a surface density equal to the measured column density of the LA II region,  $\Sigma_f \approx 0.56 M_{\odot} \text{pc}^{-2}$  such that

$$\Sigma_{\text{LA}}(t) = \exp \left[ \frac{(\ln \Sigma_f - \ln \Sigma_0)}{\tau} t + \ln \Sigma_f \right] \quad (10)$$

where again  $\tau$  is the age of *PW 1*,  $t_1 = -\tau$ , and  $t_2 = 0$ .

As mentioned above, we also allow for momentum coupling between the MW disk and the LA II gas as it passes through the Galactic midplane. To take this momentum coupling into account, we add an additional acceleration to the orbit integration,  $\mathbf{a}_{\text{coupling}}$ , defined to point in the direction of Galactic rotation such that

$$\mathbf{a}_{\text{coupling}} = \alpha \hat{\mathbf{v}}_{\text{rot}}(\mathbf{x}) e^{-\frac{1}{2} \frac{z^2}{\sigma_z(R)^2}} \quad (11)$$

where  $\alpha$  is a free parameter that determines the magnitude of the coupling,  $\hat{\mathbf{v}}_{\text{rot}}(\mathbf{x})$  is a unit vector that points in the direction of Galactic rotation at the position  $\mathbf{x}$ , and the Gaussian in height,  $z$ , makes this operate only when the gas orbit is close to the Galactic plane.

We next allow the scale densities,  $n_{0,h}$  and  $n_{0,d}$ , and the momentum coupling parameter,  $\alpha$ , to vary and fit for the values of these parameters that best reproduce the observed position and velocity offsets between *PW 1* and the LA II gas. We define a fiducial point in  $L_{\text{MS}}$ ,  $B_{\text{MS}}$ ,  $V_{\text{hel}}$  to set the present-day location of the densest LA II gas (see Section 4.3) that could have plausibly formed *PW 1*:

$$L_{\text{MS}} = 53.7^\circ \quad (12)$$

$$B_{\text{MS}} = -11.1^\circ \quad (13)$$

$$V_{\text{hel}} = 239 \text{ km s}^{-1} \quad (14)$$

We construct a likelihood function using the above orbit integration scheme and evaluate the likelihood of the present-day (i.e. final) orbit phase-space coordinates relative to the fiducial point defined previously. We assume a Gaussian tolerance of  $\sigma_{\text{LB}} = 0.5^\circ$  for  $L_{\text{MS}}$  and  $B_{\text{MS}}$ , and  $\sigma_v = 1 \text{ km s}^{-1}$  for  $V_{\text{hel}}$  and evaluate the likelihood as

$$\begin{aligned} 3p(L_{\text{MS}}, B_{\text{MS}}, V_{\text{hel}} | n_{0,h}, n_{0,d}, \alpha) = \\ \mathcal{N}(L_{\text{orbit}} | L_{\text{MS}}, \sigma_{\text{LB}}^2) \\ \times \mathcal{N}(B_{\text{orbit}} | B_{\text{MS}}, \sigma_{\text{LB}}^2) \\ \times \mathcal{N}(V_{\text{orbit}} | V_{\text{hel}}, \sigma_v^2) \end{aligned} \quad (15)$$

where  $\mathcal{N}(\cdot | \mu, \sigma^2)$  represents the normal distribution with mean  $\mu$  and variance  $\sigma^2$ . In practice, we implement this function (programmatically) over the log values of the three parameters (because they must be positive), but we assume uniform priors in the parameter values over the domain  $(a, b) = (e^{-30}, e^5)$  for each parameter such that the prior distribution is

$$p(n_{0,h}, n_{0,d}, \alpha) = \mathcal{U}(n_{0,h} | a, b) \mathcal{U}(n_{0,d} | a, b) \mathcal{U}(\alpha | a, b) \quad (16)$$

where  $\mathcal{U}(\cdot | a, b)$  is the uniform distribution defined over the domain  $(a, b)$ .

We first optimize the log-posterior,

$$\begin{aligned} \ln p(n_{0,h}, n_{0,d}, \alpha | L_{\text{MS}}, B_{\text{MS}}, V_{\text{hel}}) \propto \\ \ln p(L_{\text{MS}}, B_{\text{MS}}, V_{\text{hel}} | n_{0,h}, n_{0,d}, \alpha) \\ + \ln p(n_{0,h}, n_{0,d}, \alpha) \end{aligned}$$

using the BFGS algorithm (implemented in `scipy`, Byrd et al. 1995; Jones et al. 2001–) and then we use these optimal parameter values as initial conditions to run a Markov Chain Monte Carlo (MCMC) sampling of the posterior probability distribution (pdf) of our parameters. We use an affine-invariant, ensemble MCMC sampler (`emcee`; Foreman-Mackey et al. 2013; Goodman & Weare 2010); we run with 64 walkers for 512 “burn-in” steps (that are discarded) and then run for an additional

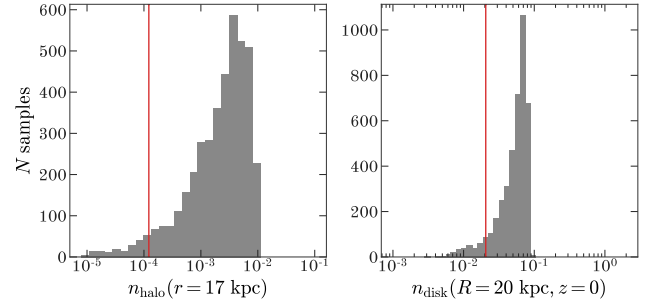


**Figure 12.** Posterior samples from the ram pressure orbit analysis, transformed to values of the inferred halo gas density at  $r = 17 \text{ kpc}$   $n_{\text{halo}}(17)$  (left panel) and disk gas density (right panel) at the midplane at  $(R, z) = (20, 0) \text{ kpc}$ ,  $n_{\text{disk}}(20, 0)$ . Vertical red lines show the values from the default Milky Way model from Miller & Bregman (2013) and Kalberla & Kerp (2009).

1024 steps. We thin the resulting chains by taking every 4th step, and combine the parameter samplings from all thinned chains. Figure 12 shows histograms of posterior samples transformed into values of the halo gas density evaluated at the orbital pericenter,  $n_{\text{halo}}(17 \text{ kpc})$ , and the disk gas density at the midplane at  $n_{\text{disk}}(20 \text{ kpc}, 0)$ . The posterior values of the coupling coefficient,  $\alpha$ , were all  $< e^{-12}$  and thus consistent with zero.

The best-fit parameters require a somewhat larger halo and disk gas densities than the fiducial MW gas density models from Miller & Bregman (2013) and Kalberla & Kerp (2009). In detail, we find

$$n_{\text{halo}}(17 \text{ kpc}) = 2.7_{-2.0}^{+3.4} \times 10^{-3} \text{ atoms cm}^{-3} \quad (17)$$

$$n_{\text{disk}}(20 \text{ kpc}, 0) = 6.0_{-2.0}^{+1.5} \times 10^{-2} \text{ atoms cm}^{-3} \quad (18)$$

as compared to the fiducial values  $n_{\text{halo}, \text{M13}}(17 \text{ kpc}) = 1.2 \times 10^{-4} \text{ atoms cm}^{-3}$  and  $n_{\text{disk}, \text{K09}}(20 \text{ kpc}, 0) = 2 \times 10^{-2} \text{ atoms cm}^{-3}$ . However, the goal of this analysis is only to illustrate that the observed offsets could plausibly be described by ram pressure, and that the inferred MW halo and disk gas densities needed to explain the magnitude of the ram pressure drag are reasonable. In doing this, we neglect more complex density evolution of the LA gas, assume that the LA II gas, at least around the *PW 1* birthplace, acts like a cloud (rather than a dissolving and morphologically-varying gas filament), and assume that no supernovae (SNe) have impacted the orbital energy of the gas. Still, this result motivates more detailed simulation of the interaction between the LA and the MW.

## 5. DISCUSSION

The distance, radial velocity, metallicity, and orbit suggest that not only is *PW 1* associated with LA II,

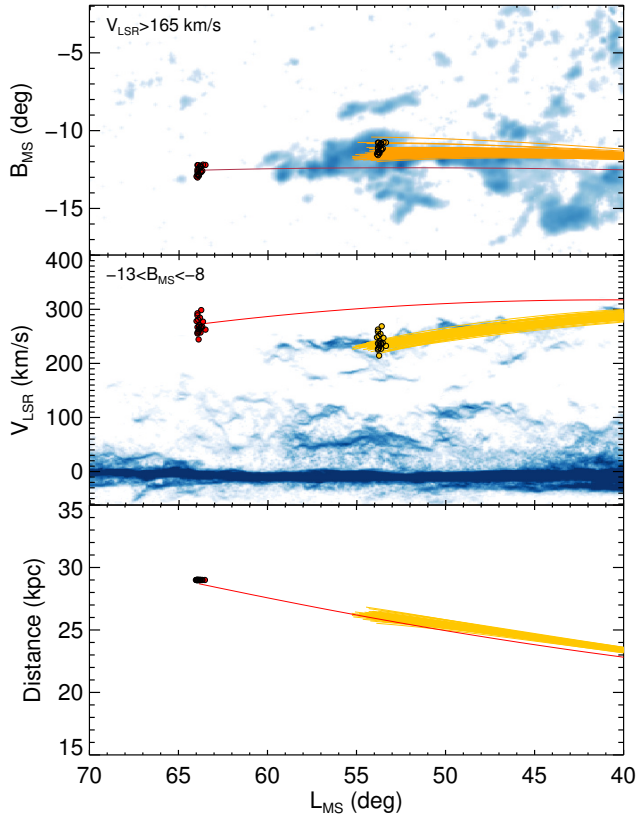


**Figure 13.** The orbits of both the mean *PW 1* stars and the originating gas that experienced ram pressure. (Top)  $B_{\text{MS}}$  vs.  $L_{\text{MS}}$ , (middle)  $V_{\text{LSR}}$  vs.  $L_{\text{MS}}$ , and (bottom) distance vs.  $L_{\text{MS}}$ . The red line is the *PW 1* orbit with no ram pressure, while the orange lines show 64 orbits of the *PW 1* birth cloud drawn from the MCMC posterior distributions of the parameters.

but that it is also associated with the MCs and MS. The association of *PW 1* with LA II permits a more nuanced view of the LA than has previously been feasible. Not only does *PW 1* provide a distance measurement to the LA, but it also constrains its chemical, orbital, and dynamical properties, such as how it is affected by ram pressure from the MW hot halo. At the same time, affiliating *PW 1* with the LA gas also explains some of its properties, as discussed below.

### 5.1. The Spatial Morphology of *PW 1*

One of the mysteries of *PW 1* is its unusual spatial shape and elongated distribution. However, the spatial correlation of the HI LA II gas and the *PW 1* stars suggests a natural explanation for this. The *PW 1* stars do not represent one single cluster that has disrupted but rather is likely the outcome of multiple star formation events associated with high-density HI clumps in LA II. This is a common feature observed in jellyfish galaxies

experiencing ram pressure in galaxy clusters. Therefore, it might be more appropriate to call *PW 1* a star formation “complex” or association rather than a star cluster in the traditional sense.

### 5.2. Origin of the Leading Arm

The mean metallicity of *PW 1* of  $\approx -1.23$  is similar to the measured metallicity of the LA ( $[O/H] \approx -1.16$ ; Fox et al. 2018), the Magellanic Bridge ( $\approx -1.0$ ; Lehner et al. 2008) and the trailing MS ( $\approx -1.2$ ; Fox et al. 2013a). There is a large range in the measured metallicities of MW HI high-velocity clouds (HVCs; Wakker 2001), and, therefore, the similarity of the metallicities in these distinct systems supports the notion that the LA, MB, and MS all share a common origin. These metallicities are also consistent with the metallicity of the SMC  $\sim 2$  Gyr ago. Therefore, all of these gas structures associated with the MCs likely originated mainly from the SMC from the same tidal event about 2 Gyr ago.

Despite the similar metallicities among the gas structures, the origin of the MS and LA are still debated. This is mainly because (1) the observational data is far from complete – e.g., the metallicity measurements are limited to small number of sightlines, and (2) there are some observed features that cannot be easily explained by the sole SMC origin (e.g., Fox et al. 2013b). One of the recent theoretical studies Paridy et al. (2018) argued that both the LMC and SMC contributed to create the LA and MS gas features. However, another recent MS simulation work by Tepper-García & Bland-Hawthorn (2018) suggested that the LA gas does not originate in the MCs because the ram pressure from the MW hot halo gas would prevent the gas from reaching its present position. If *PW 1* is indeed affiliated with LA II, as we suggest here, then there is now observational evidence that the impact of ram pressure is overestimated in Tepper-García & Bland-Hawthorn (2018). The key discriminant is the assumed  $\rho_{\text{MW}}$  in Tepper-García & Bland-Hawthorn (2018) versus what we infer from our scenario for *PW 1*.

### 5.3. No Natal Gas Disruption?

The conditions for triggering star formation in the LA is not well understood. Based on the fact that *PW 1* is the only known stellar component to date that is likely associated with LA II, the birth cloud of *PW 1* must have satisfied very special star formation conditions in the LA while passing through the Galactic midplane. Aside from the unknown star formation conditions of *PW 1*, there is another mystery: How has the morphology of the *PW 1* birth cloud remained mostly intact?

Our analysis in §4.3 shows that the present-day spatial distribution of the associated HI gas resembles that of the *PW 1* stars across  $\sim 2.5$  kpc.

A gas cloud that forms a young star cluster is disrupted when the first SN occurs. The SN-explosions effectively act to distort the original spatial correlations between the gas and stars by injecting radiative and mechanical energy into the birth gas. Similar spatial distributions of the stars and gas after the shift of  $(-10.15^\circ, +1.44^\circ)$  in  $(L_{\text{MS}}, B_{\text{MS}})$  indicate that *PW 1* birth cloud did not undergo significant gas removal and/or gas destruction period at all, or at least not at significant level. This might only be possible in the absence of stellar feedback in the *PW 1* birth cloud.

One way to avoid the impact of stellar feedback on the gas cloud is not to have SN events. To test the possibility that no SNe occurred in *PW 1*, we compute the expected number of SN explosions in *PW 1*-like star clusters. Based on the present-day mass, age, and metallicity of *PW 1*, PARSEC stellar evolutionary models suggest that the initial mass of *PW 1* is  $\sim 1800 M_\odot$ . We then simulate a  $1800 M_\odot$  star cluster 20000 times assuming a Kroupa IMF and count the number of SN explosion events in each star cluster. If we assume that all stars more massive than  $8 M_\odot$  explode as Type II SNe, then all of the simulated *PW 1*-like clusters produce at least 1 core-collapse SN  $\sim 3$  Myr (a typical lifetime of a  $8 M_\odot$  star) after its birth. Thus, this scenario is unsuitable to explain the similar present-day spatial pattern between the *PW 1* and its birth cloud.

Another way to avoid the gas disruption by stellar feedback is to spatially decouple the birth cloud and the newly formed stars before the first SN explosion. Over 3 Myr, the *PW 1* stars were able to travel  $\sim 14.3$  pc (corresponding to  $\sim 50$  yr) away from the birth cloud based on the orbital calculation in §4.5. This spatial decoupling due to ram pressure might prevent the *PW 1* birth cloud from being significantly disrupted by stellar feedback. If the *PW 1* stars and gas were indeed decoupled before the first SN explosion, our assumption about no effect of SN on the stellar motions (§4.5) can be naturally justified.

## 6. SUMMARY

We have obtained high-resolution Magellan+MIKE spectra of 28 candidates of *PW 1*, a young stellar association in the region of the Leading Arm. Our sample allows us to draw some important conclusions about the properties and origin of both *PW 1* and the Leading Arm:

1. *PW 1* has a median metallicity of  $[\text{Fe}/\text{H}] = -1.23$  with a small scatter of 0.06 dex and an inferred ve-

locity of  $V_{\text{LSR}} = 273.4 \text{ km s}^{-1}$  with a dispersion of  $11.0 \text{ km s}^{-1}$ . The derived stellar parameters ( $T_{\text{eff}}$ ,  $\log g$ ,  $[\text{Fe}/\text{H}]$ ) are consistent with the young, metal-poor isochrone (116 Myr and  $[\text{Fe}/\text{H}] = -1.1$ ) that was determined in Paper I using photometry for proper-motion selected members.

2. There is a strong correlation between the spatial patterns of the *PW 1* stars and the high-density HI clumps of LA II with an offset of  $(-10.15^\circ, +1.55^\circ)$  in  $(L_{\text{MS}}, B_{\text{MS}})$  (Figure 10).
3. Due to the similarity of metallicity, velocity, spatial patterns, and the distance of *PW 1*, we find that *PW 1* likely originated from the LA II complex of the Magellanic Stream.
4. The orbit and metallicity of *PW 1* and LA II associate them with the Magellanic Clouds and Magellanic Stream, in contrast to some recent claims to the contrary.
5. Using an orbital analysis of the *PW 1* stars and the LA II gas, taking into account ram pressure from a MW model, we constrain the halo gas density at the orbital pericenter of *PW 1* to be  $n_{\text{halo}}(17 \text{ kpc}) = 2.7^{+3.4}_{-2.0} \times 10^{-3} \text{ atoms cm}^{-3}$  and the disk gas density at the midplane at 20 kpc to be  $n_{\text{disk}}(20 \text{ kpc}, 0) = 6.0^{+1.5}_{-2.0} \times 10^{-2} \text{ atoms cm}^{-3}$ . We also predict that the current distance of the *PW 1* birth cloud in LA II is 27 kpc.

Future work will investigate the detailed chemical abundances of *PW 1* and how it compares to the Magellanic Clouds.

We thank Carlos Allende Prieto for sharing his Synspec IDL wrapper and utility software. We also thank Andy Casey for general help in running his Cannon software. We thank Michael Strauss for organizing and scheduling our Magellan time. APW thanks Stephanie Tonnesen and Elena D’Onghia for helpful conversations. DB and NWE thank Jane Luu for valuable advice and assistance in using the Goodman spectrograph at the SOAR telescope. We thank Andrew Fox and Kat Barger for useful discussions on the origin of *PW 1* and the metallicity variations in the Leading Arm. We thank the anonymous referee for useful comments that improved the manuscript. Support for this work was provided by NASA through Hubble Fellowship grant #51386.01 awarded to R.L.B. by the Space Telescope Science Institute, which is operated by the Association of Universities for Research in Astronomy, Inc., for NASA, under contract NAS 5-26555. This work presents results from

the European Space Agency (ESA) space mission Gaia. Gaia data are being processed by the Gaia Data Processing and Analysis Consortium (DPAC). Funding for the DPAC is provided by national institutions, in particular the institutions participating in the Gaia MultiLateral Agreement (MLA). The Gaia mission website is <https://www.cosmos.esa.int/gaia>. The Gaia archive website is <https://archives.esac.esa.int/gaia>. This paper includes data gathered with the 6.5 meter Magellan Telescopes located at Las Campanas Observatory, Chile.

Based on observations obtained at the Southern Astrophysical Research (SOAR) telescope, which is a joint project of the Ministério da Ciência, Tecnologia, In-

ovações e Comunicações (MCTIC) do Brasil, the U.S. National Optical Astronomy Observatory (NOAO), the University of North Carolina at Chapel Hill (UNC), and Michigan State University (MSU).

*Facility:* Magellan:Clay (MIKE)

*Facility:* SOAR (Goodman)

*Software:* CarPy: MIKE (Kelson et al. 2000; Kelson 2003), *Synspec* (Hubeny & Lanz 2017), *IRAF* (Tody 1986, 1993), *The Cannon* (Ness et al. 2017; Casey et al. 2012), *Astropy* (The Astropy Collaboration et al. 2018), *gala* (Price-Whelan 2017), *IPython* (Pérez & Granger 2007), *matplotlib* (Hunter 2007), *numpy* (Walt et al. 2011), *scipy* (Jones et al. 2001–)

## REFERENCES

- Bernstein, R., Shectman, S. A., Gunnels, S. M., Mochnacki, S., & Athey, A. E. 2003, in Proc. SPIE, Vol. 4841, Instrument Design and Performance for Optical/Infrared Ground-based Telescopes, ed. M. Iye & A. F. M. Moorwood, 1694–1704
- Besla, G., Kallivayalil, N., Hernquist, L., et al. 2007, *ApJ*, 668, 949
- . 2012, *MNRAS*, 421, 2109
- Bovy, J. 2015, The Astrophysical Journal Supplement Series, 216, 29
- Brown, A. G. A., Vallenari, A., Prusti, T., & de Bruijne, J. H. J. 2018, *Astronomy & Astrophysics*, doi:10.1051/0004-6361/201833051
- Brueck, M. T., & Hawkins, M. R. S. 1983, *A&A*, 124, 216
- Brüns, C., Kerp, J., Staveley-Smith, L., et al. 2005, *A&A*, 432, 45
- Byrd, R. H., Lu, P., Nosedal, J., & Zhu, C. 1995, *SIAM J. Sci. Comput.*, 16, 1190.  
<http://dx.doi.org/10.1137/0916069>
- Carpenter, B., Gelman, A., Hoffman, M., et al. 2017, *Journal of Statistical Software, Articles*, 76, 1.  
<https://www.jstatsoft.org/v076/i01>
- Casetti-Dinescu, D. I., Moni Bidin, C., Girard, T. M., et al. 2014, *ApJL*, 784, L37
- Casey, A. R., Hogg, D. W., Ness, M., et al. 2016, arXiv e-prints, arXiv:1603.03040
- Casey, A. R., Keller, S. C., & Da Costa, G. 2012, *AJ*, 143, 88
- Choi, Y., Nidever, D. L., Olsen, K., et al. 2018a, *ApJ*, 866, 90
- . 2018b, *ApJ*, 869, 2
- Clemens, J. C., Crain, J. A., & Anderson, R. 2004, in Society of Photo-Optical Instrumentation Engineers (SPIE) Conference Series, Vol. 5492, Proc. SPIE, ed. A. F. M. Moorwood & M. Iye, 331–340
- Connors, T. W., Kawata, D., & Gibson, B. K. 2006, *MNRAS*, 371, 108
- Delhaye, J. 1965, *Solar Motion and Velocity Distribution of Common Stars*, 61
- Diaz, J. D., & Bekki, K. 2012, *ApJ*, 750, 36
- D’Onghia, E., & Fox, A. J. 2016, *ARA&A*, 54, 363
- Dorman, B., Rood, R. T., & O’Connell, R. W. 1993, *ApJ*, 419, 596
- Dormand, J., & Prince, P. 1980, *Journal of Computational and Applied Mathematics*, 6, 19 . <http://www.sciencedirect.com/science/article/pii/0771050X80900133>
- Erkal, D., Belokurov, V., Laporte, C. F. P., et al. 2019, *MNRAS*, 487, 2685
- For, B.-Q., Staveley-Smith, L., & McClure-Griffiths, N. M. 2013, *ApJ*, 764, 74
- Foreman-Mackey, D., Hogg, D. W., Lang, D., & Goodman, J. 2013, *Publications of the Astronomical Society of the Pacific*, 125, 306
- Fox, A. J., Richter, P., Wakker, B. P., et al. 2013a, *ApJ*, 772, 110
- . 2013b, *The Messenger*, 153, 28
- Fox, A. J., Wakker, B. P., Smoker, J. V., et al. 2010, *ApJ*, 718, 1046
- Fox, A. J., Barger, K. A., Wakker, B. P., et al. 2018, *ApJ*, 854, 142
- Gardiner, L. T., & Noguchi, M. 1996, *MNRAS*, 278, 191
- Goodman, J., & Weare, J. 2010, *Communications in Applied Mathematics and Computational Science*, 5, 65

- Gordon, M. A. 1976, *Methods of Experimental Physics*, 12, 277
- Guhathakurta, P., & Reitzel, D. B. 1998, in *Astronomical Society of the Pacific Conference Series*, Vol. 136, Galactic Halos, ed. D. Zaritsky, 22
- Harris, J., & Zaritsky, D. 2004, *AJ*, 127, 1531
- . 2009, *AJ*, 138, 1243
- Helmi, A., van Leeuwen, F., McMillan, P., & DPAC. 2018, *Astronomy & Astrophysics*, doi:10.1051/0004-6361/201832698
- Hernquist, L. 1990, *ApJ*, 356, 359
- Homan, M. D., & Gelman, A. 2014, *J. Mach. Learn. Res.*, 15, 1593.  
<http://dl.acm.org/citation.cfm?id=2627435.2638586>
- Hubeny, I., & Lanz, T. 2011, *Synspec: General Spectrum Synthesis Program*, , ascl:1109.022
- . 2017, arXiv e-prints, arXiv:1706.01859
- Hunter, J. D. 2007, *Computing in Science and Engineering*, 9, 90
- Jones, E., Oliphant, T., Peterson, P., et al. 2001–, *SciPy: Open source scientific tools for Python*, , .  
<http://www.scipy.org/>
- Kalberla, P. M. W., & Kerp, J. 2009, *ARA&A*, 47, 27
- Kallivayalil, N., van der Marel, R. P., Alcock, C., et al. 2006, *ApJ*, 638, 772
- Kallivayalil, N., van der Marel, R. P., Besla, G., Anderson, J., & Alcock, C. 2013, *ApJ*, 764, 161
- Kelson, D. D. 2003, *PASP*, 115, 688
- Kelson, D. D., Illingworth, G. D., van Dokkum, P. G., & Franx, M. 2000, *ApJ*, 531, 159
- Kunkel, W. E., Irwin, M. J., & Demers, S. 1997, *A&AS*, 122, 463
- Laporte, C. F. P., Gómez, F. A., Besla, G., Johnston, K. V., & Garavito-Camargo, N. 2018, *MNRAS*, 473, 1218
- Lehner, N., Howk, J. C., Keenan, F. P., & Smoker, J. V. 2008, *ApJ*, 678, 219
- Lu, L., Savage, B. D., Sembach, K. R., et al. 1998, *AJ*, 115, 162
- Majewski, S. R., Nidever, D. L., Muñoz, R. R., et al. 2009, in *IAU Symposium*, Vol. 256, *The Magellanic System: Stars, Gas, and Galaxies*, ed. J. T. Van Loon & J. M. Oliveira, 51–56
- Mastropietro, C., Moore, B., Mayer, L., Wadsley, J., & Stadel, J. 2005, *MNRAS*, 363, 509
- Mathewson, D. S., Cleary, M. N., & Murray, J. D. 1974, *ApJ*, 190, 291
- McClure-Griffiths, N. M., Staveley-Smith, L., Lockman, F. J., et al. 2008, *ApJL*, 673, L143
- McClure-Griffiths, N. M., Pisano, D. J., Calabretta, M. R., et al. 2009, *ApJS*, 181, 398
- Miller, M. J., & Bregman, J. N. 2013, *ApJ*, 770, 118
- Muñoz, R. R., Majewski, S. R., Zaggia, S., et al. 2006, *ApJ*, 649, 201
- Ness, M., Hogg, D. W., Rix, H.-W., Ho, A. Y. Q., & Zasowski, G. 2015, *ApJ*, 808, 16
- Ness, M., Rix, H., Hogg, D. W., et al. 2017, ArXiv e-prints, arXiv:1701.07829
- Nidever, D. L., Majewski, S. R., & Butler Burton, W. 2008, *ApJ*, 679, 432
- Nidever, D. L., Majewski, S. R., Butler Burton, W., & Nigra, L. 2010, *ApJ*, 723, 1618
- Nidever, D. L., Majewski, S. R., Muñoz, R. R., et al. 2011, *ApJL*, 733, L10
- Nidever, D. L., Hasselquist, S., Hayes, C. R., et al. 2019a, arXiv e-prints, arXiv:1901.03448
- Nidever, D. L., Olsen, K., Choi, Y., et al. 2019b, *ApJ*, 874, 118
- Noël, N. E. D., Conn, B. C., Read, J. I., et al. 2015, *MNRAS*, 452, 4222
- Oh, S., Price-Whelan, A. M., Hogg, D. W., Morton, T. D., & Spergel, D. N. 2017, *AJ*, 153, 257
- Olano, C. A. 2004, *A&A*, 423, 895
- Olsen, K. A. G., Zaritsky, D., Blum, R. D., Boyer, M. L., & Gordon, K. D. 2011, *ApJ*, 737, 29
- Pagel, B. E. J., & Tautvaisiene, G. 1998, *MNRAS*, 299, 535
- Pardy, S. A., D’Onghia, E., & Fox, A. J. 2018, *ApJ*, 857, 101
- Patel, E., Besla, G., & Sohn, S. T. 2017, *MNRAS*, 464, 3825
- Pérez, F., & Granger, B. E. 2007, *Computing in Science and Engineering*, 9, 21. <http://ipython.org>
- Philip, A. G. D. 1976a, in *BAAS*, Vol. 8, 352
- Philip, A. G. D. 1976b, in *BAAS*, Vol. 8, 532
- Price-Whelan, A. M. 2017, *The Journal of Open Source Software*, 2, 388
- Price-Whelan, A. M., Nidever, D. L., Choi, Y., et al. 2018, arXiv e-prints, arXiv:1811.05991
- Putman, M. E., Peek, J. E. G., & Jounge, M. R. 2012, *ARA&A*, 50, 491
- Putman, M. E., Staveley-Smith, L., Freeman, K. C., Gibson, B. K., & Barnes, D. G. 2003, *ApJ*, 586, 170
- Putman, M. E., Gibson, B. K., Staveley-Smith, L., et al. 1998, *Nature*, 394, 752
- Recillas-Cruz, E. 1982, *MNRAS*, 201, 473
- Richter, P., Fox, A. J., Wakker, B. P., et al. 2018, *ApJ*, 865, 145
- . 2013, *ApJ*, 772, 111
- Russell, S. C., & Dopita, M. A. 1992, *ApJ*, 384, 508
- Schönrich, R., Binney, J., & Dehnen, W. 2010, *MNRAS*, 403, 1829

- Stanimirović, S., Hoffman, S., Heiles, C., et al. 2008, *ApJ*, 680, 276
- Tepper-García, T., & Bland-Hawthorn, J. 2018, *MNRAS*, 478, 5263
- The Astropy Collaboration, Price-Whelan, A. M., Sipőcz, B. M., et al. 2018, *ArXiv e-prints*, arXiv:1801.02634
- Tody, D. 1986, in *Society of Photo-Optical Instrumentation Engineers (SPIE) Conference Series*, Vol. 627, *Proc. SPIE*, ed. D. L. Crawford, 733
- Tody, D. 1993, in *Astronomical Society of the Pacific Conference Series*, Vol. 52, *Astronomical Data Analysis Software and Systems II*, ed. R. J. Hanisch, R. J. V. Brissenden, & J. Barnes, 173
- Vollmer, B., Cayatte, V., Balkowski, C., & Duschl, W. J. 2001, *ApJ*, 561, 708
- Wakker, B. P. 2001, *ApJS*, 136, 463
- Walt, S. v. d., Colbert, S. C., & Varoquaux, G. 2011, *Computing in Science and Engg.*, 13, 22.  
<http://dx.doi.org/10.1109/MCSE.2011.37>
- Wannier, P., Wrixon, G. T., & Wilson, R. W. 1972, *A&A*, 18, 224
- Weisz, D. R., Dolphin, A. E., Skillman, E. D., et al. 2013, *MNRAS*, 431, 364
- Wong, T., Hughes, A., Ott, J., et al. 2011, *ApJS*, 197, 16
- Zhang, L., Casetti-Dinescu, D. I., Moni Bidin, C., et al. 2019, *ApJ*, 871, 99
- Zivick, P., Kallivayalil, N., van der Marel, R. P., et al. 2018, *ApJ*, 864, 55

Table 1. *PW 1* Spectroscopic Results

| Name   | Gaia ID<br>(J2000)  | RA         | DEC         | G     | G <sub>BP</sub> -G <sub>RP</sub><br>(mag) | $\mu_{RA}$<br>(mas yr <sup>-1</sup> ) | $\mu_{DEC}$ | S/N  | $V_{LSR}$<br>(km s <sup>-1</sup> ) | $\sigma_V$ | T <sub>eff</sub><br>(K) | $\sigma_{T,eff}$ | log g | $\sigma_{log g}$<br>(dex) | [Fe/H] | $\sigma_{[Fe/H]}$<br>(dex) |
|--------|---------------------|------------|-------------|-------|---|---------------------------------------|-------------|------|------------------------------------|------------|-------------------------|------------------|-------|---------------------------|--------|----------------------------|
| PW1-00 | 3466763224691512064 | 11:55:31.8 | -33:09:11.6 | 15.10 | -0.11                                     | -0.58                                 | 0.46        | 11.8 | 239.7                              | 7.3        | 14465                   | 766              | 2.25  | 0.12                      | -0.81  | 0.32                       |
| PW1-01 | 3480054567924428032 | 11:56:00.4 | -29:28:48.9 | 16.30 | -0.21                                     | -0.45                                 | 0.42        | 14.2 | 257.1                              | 6.7        | 17326                   | 873              | 3.38  | 0.13                      | -0.82  | 0.32                       |
| PW1-02 | 3480064910205689088 | 11:56:18.3 | -29:19:20.8 | 16.39 | -0.24                                     | -0.85                                 | 0.55        | 12.4 | 255.3                              | 7.3        | 16340                   | 1000             | 3.20  | 0.16                      | -1.06  | 0.35                       |
| PW1-03 | 3480053399693321984 | 11:56:12.0 | -29:31:44.4 | 16.71 | -0.23                                     | -0.37                                 | 0.50        | 4.3  | 298.5                              | 20.0       | 17436                   | 2041             | 3.22  | 0.36                      | -0.33  | 0.57                       |
| PW1-04 | 3486242378847130624 | 12:00:11.5 | -27:59:50.4 | 16.78 | -0.17                                     | -0.76                                 | 0.45        | 8.8  | 235.1                              | 11.3       | 14654                   | 953              | 3.38  | 0.19                      | -1.11  | 0.30                       |
| PW1-05 | 3479870124848931200 | 11:57:20.8 | -29:27:45.2 | 16.84 | -0.20                                     | -0.58                                 | 0.55        | 16.1 | 262.7                              | 5.3        | 17534                   | 548              | 3.76  | 0.09                      | -1.04  | 0.18                       |
| PW1-06 | 3479874106283037568 | 11:56:56.3 | -29:25:11.6 | 16.84 | -0.20                                     | -0.71                                 | 0.57        | 29.1 | 259.0                              | 3.3        | 15567                   | 263              | 3.77  | 0.05                      | -1.25  | 0.12                       |
| PW1-07 | 3480052712498583424 | 11:55:46.3 | -29:33:56.9 | 16.87 | -0.24                                     | -0.43                                 | 0.50        | 30.6 | 267.9                              | 2.7        | 17321                   | 315              | 3.51  | 0.05                      | -1.26  | 0.12                       |
| PW1-08 | 3486167027940903296 | 11:56:04.8 | -28:28:38.8 | 16.95 | -0.21                                     | -0.47                                 | 0.59        | 32.0 | 274.9                              | 2.7        | 17930                   | 321              | 3.64  | 0.05                      | -1.32  | 0.10                       |
| PW1-09 | 3480071644714348032 | 11:55:41.7 | -29:17:32.5 | 17.01 | -0.23                                     | -0.53                                 | 0.46        | 29.3 | 266.9                              | 3.3        | 17878                   | 350              | 3.62  | 0.05                      | -1.24  | 0.12                       |
| PW1-10 | 3479874690398598784 | 11:57:09.5 | -29:21:50.6 | 17.09 | -0.18                                     | -0.54                                 | 0.40        | 27.2 | 288.7                              | 4.0        | 15805                   | 296              | 3.64  | 0.06                      | -1.16  | 0.14                       |
| PW1-11 | 3485879024613971328 | 11:57:42.5 | -29:20:32.8 | 17.14 | -0.12                                     | 0.22                                  | 0.42        | 22.7 | 278.2                              | 4.7        | 14561                   | 329              | 3.60  | 0.07                      | -1.17  | 0.15                       |
| PW1-12 | 3480036975738300800 | 11:53:53.6 | -29:38:55.3 | 17.17 | -0.17                                     | -0.49                                 | 0.47        | 23.4 | 262.4                              | 4.0        | 16105                   | 372              | 3.66  | 0.07                      | -1.25  | 0.14                       |
| PW1-13 | 3467765189021964544 | 12:00:18.7 | -30:14:30.8 | 17.19 | -0.16                                     | -0.23                                 | 0.30        | 19.9 | 341.6                              | 5.3        | 17216                   | 451              | 4.19  | 0.07                      | -1.15  | 0.17                       |
| PW1-14 | 3480121844292017920 | 11:54:23.4 | -29:15:42.0 | 17.42 | -0.22                                     | -0.40                                 | 0.44        | 24.2 | 280.7                              | 4.0        | 17254                   | 401              | 3.78  | 0.06                      | -1.24  | 0.14                       |
| PW1-15 | 3480049757560914944 | 11:54:25.0 | -29:23:44.4 | 17.54 | -0.20                                     | -0.50                                 | 0.21        | 32.9 | 267.2                              | 2.7        | 17472                   | 283              | 3.67  | 0.05                      | -1.18  | 0.09                       |
| PW1-16 | 3480046557809199616 | 11:54:46.1 | -29:25:33.5 | 17.57 | -0.22                                     | -0.54                                 | 0.45        | 37.7 | 266.4                              | 2.7        | 15726                   | 225              | 3.31  | 0.04                      | -1.16  | 0.11                       |
| PW1-17 | 3480070957519575552 | 11:55:27.6 | -29:21:43.8 | 17.59 | -0.17                                     | -0.48                                 | 0.27        | 37.8 | 268.3                              | 2.7        | 16894                   | 235              | 3.66  | 0.04                      | -1.27  | 0.08                       |
| PW1-18 | 3479762991184812544 | 11:57:32.4 | -30:14:56.6 | 17.67 | -0.19                                     | -1.00                                 | 0.36        | 38.1 | 275.9                              | 2.7        | 15871                   | 218              | 3.62  | 0.04                      | -1.25  | 0.08                       |
| PW1-19 | 3486175647939287680 | 11:57:29.7 | -28:29:54.7 | 17.70 | -0.12                                     | -0.22                                 | 0.29        | 31.5 | 257.7                              | 2.7        | 13979                   | 224              | 3.49  | 0.05                      | -1.20  | 0.10                       |
| PW1-20 | 3479873354664338688 | 11:57:09.4 | -29:25:47.3 | 17.69 | -0.07                                     | -0.61                                 | 0.37        | 29.8 | 244.3                              | 4.0        | 13609                   | 210              | 3.82  | 0.05                      | -1.22  | 0.10                       |
| PW1-21 | 3486267147922619136 | 12:00:22.2 | -27:56:54.3 | 17.74 | -0.18                                     | -0.43                                 | 0.18        | 31.6 | 289.6                              | 2.7        | 16060                   | 303              | 3.38  | 0.05                      | -1.28  | 0.11                       |
| PW1-22 | 3480047141924659456 | 11:53:57.4 | -29:30:37.4 | 17.75 | -0.18                                     | -0.40                                 | 0.40        | 28.5 | 277.2                              | 3.3        | 15402                   | 280              | 3.73  | 0.05                      | -1.28  | 0.11                       |
| PW1-23 | 3480049856344140288 | 11:54:37.3 | -29:22:36.4 | 17.80 | -0.06                                     | -0.53                                 | 0.61        | 31.9 | 284.5                              | 2.7        | 15845                   | 285              | 3.35  | 0.05                      | -1.23  | 0.12                       |
| PW1-24 | 3485874897149344256 | 11:57:58.3 | -29:24:47.2 | 17.79 | -0.12                                     | -0.51                                 | 0.44        | 29.9 | 257.2                              | 3.3        | 15246                   | 291              | 3.47  | 0.06                      | -1.19  | 0.12                       |
| PW1-25 | 3480070510842975104 | 11:55:07.5 | -29:21:14.9 | 17.82 | -0.08                                     | -0.71                                 | 0.37        | 29.3 | 271.2                              | 4.0        | 13570                   | 201              | 4.00  | 0.05                      | -1.15  | 0.10                       |
| PW1-26 | 3480122325328358144 | 11:54:25.7 | -29:13:24.8 | 18.30 | -0.23                                     | -0.42                                 | 0.45        | 21.3 | 292.6                              | 4.7        | 14914                   | 189              | 3.01  | 0.05                      | -1.21  | 0.02                       |
| PW1-27 | 3486267251001844736 | 12:00:23.1 | -27:55:21.8 | 17.94 | -0.12                                     | -0.89                                 | 0.37        | 29.3 | 270.0                              | 3.3        | 15050                   | 264              | 3.30  | 0.05                      | -1.18  | 0.05                       |